Published in final edited form as:

J Am Chem Soc. 2017 September 06; 139(35): 12209–12218. doi:10.1021/jacs.7b05800.

Manganese and Cobalt in the Nonheme Metal-binding Site of a Biosynthetic Model of Heme-Copper Oxidase Superfamily Confer Oxidase Activity through Redox-inactive Mechanism

Julian H. Reed[1], **Yelu Shi**[2], **Qianhong Zhu**[3], **Saumen Chakraborty**[4], **Evan N. Mirts**[5], **Igor D. Petrik**[6], **Ambika Bhagi-Damodaran**[7], **Matthew Ross**[8], **Pierre Moënne-Loccoz**[3,*], **Yong Zhang**[2,*], and **Yi Lu**[1,5,6,*]

[1]Department of Biochemistry, University of Illinois at Urbana-Champaign, Urbana, IL, 61801, USA

[2]Department of Biomedical Engineering, Chemistry, and Biological Sciences, Stevens Institute of Technology, Hoboken, NJ, 07030, USA

[3]Division of Environmental & Biomolecular Systems, Institute of Environmental Health, Oregon Health & Science University, Portland, OR, 97239, USA

[4]Department of Chemistry & Biochemistry, University of Mississippi, Oxford, Mississippi, 38677, USA

[5]Center for Biophysics and Quantitative Biology, University of Illinois at Urbana-Champaign, Urbana, IL, 61801, USA

[6]Department of Chemistry, University of Illinois at Urbana-Champaign, Urbana, IL, 61801, USA

[7]Department of Pharmaceutical Chemistry, University of California, San Francisco, San Francisco, CA, 94143, USA

[8]Department of Chemistry, Northwestern University, Evanston, IL, 60208, USA

Abstract

The presence of nonheme metal, such as copper and iron, in the heme-copper oxidase (HCO) superfamily is critical to the enzymatic activity of reducing O_2 to H_2O, but the exact mechanism the nonheme metal ion uses to confer and fine-tune the activity remains to be understood. We report that manganese and cobalt can bind to the same nonheme site and confer HCO activity in a heme-nonheme biosynthetic model in myoglobin. While the initial rates of O_2 reduction by the Mn, Fe and Co derivatives are similar, the percentage of reaction active species formation are 7%, 4% and 1% and the total turnovers are 5.1 ± 1.1, 13.4 ± 0.7, and 82.5 ± 2.5, respectively. These results correlate with the trends of nonheme metal-binding dissociation constants (35 μM, 22 μM

*Corresponding authors, yi-lu@illinois.edu; yong.zhang@stevens.edu; moennelo@ohsu.edu.

Associated Content

Supporting information is available, including UV-vis metal titration, WT Mb O_2 reduction rates, spectroelectrochemistry measurements, stopped-flow UV-Vis of Mn^{II}- and Co^{II}-Fe_BMb(Fe^{II}) in the presence of ascorbate, low-frequency RR, crystallographic diffraction and refinement data, and computational details. This material is available free of charge via the Internet at http://pubs.acs.org.

Notes

The authors declare no competing financial interest.

and 9 μM) closely, suggesting that tighter metal binding can prevent ROS release from the active site, lessen damage to the protein, and produce higher total turnover numbers. Detailed spectroscopic, electrochemical, and computational studies found no evidence of redox cycling of manganese or cobalt in the enzymatic reactions, and suggest that structural and electronic effects related to the presence of different nonheme metals lead to observed differences in reactivity. This study of the roles of nonheme metal ions beyond the Cu and Fe found in native enzymes has provided deeper insights into nature's choice of metal ion, and reaction mechanism, and allows for finer control of the enzymatic activity, which is a basis for design of efficient catalysts for oxygen reduction reaction for fuel cells.

TOC image

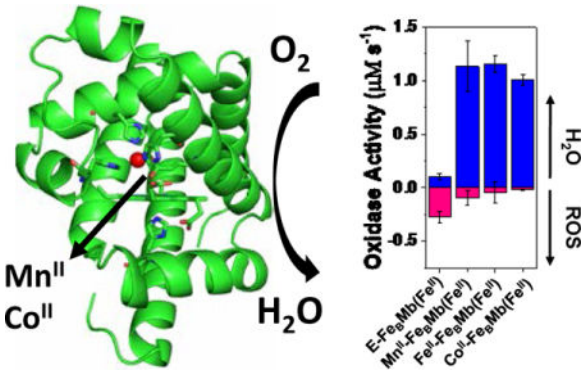

Introduction

Heme-copper oxidases (HCOs) perform the 4-electron, 4-proton reduction of O_2 to H_2O ($O_2 + 4e^- + 4H^+ \rightarrow 2H_2O$), and couple this reduction to proton pumping to generate an electrochemical gradient that is utilized to synthesize adenosine triphosphate (ATP), the biological energy currency.[1,2] Nitric oxide reductases (NORs) are structurally homologous enzymes to HCOs that carry out the 2-electron, 2-proton reduction of NO to N_2O ($2NO + 2e^- + 2H^+ \rightarrow N_2O + H_2O$), an important step in the biological denitrification process.[3] Despite the different functions, both enzymes belong to the same enzyme superfamily and contain a heme-nonheme active site, with a major difference being that HCOs contain nonheme Cu_B, while NOR contains nonheme Fe_B (Figure S1).[4–8] It is interesting to note that cross reactivity between HCOs and NORs has been observed, in which each enzyme is more reactive towards it native substrate.[9,10] Despite studies into understanding these differences in reactivity,[11,12] an open question in the field remains: why do HCOs use copper while NORs utilize nonheme iron for their respective activities. While the most direct way of addressing this question would be to replace the nonheme metal ion in either HCOs or NORs with another metal ion, such an approach has been unsuccessful in the native proteins due to both enzymes being membranous, containing multiple subunits and cofactors, as well as their overall size (~70-200kDa) and complexity; any attempt to extract the nonheme metal ion from these proteins has resulted in structurally perturbed proteins whose activity cannot be restored even after adding the native metal ion back.[13] Therefore, having a *single* protein that can bind a wide array of nonheme metal ions would be ideal for

answering such a question. Synthetic models of HCOs and NORs have been reported.[14–21] While studies of these models have provided valuable insights into structural features responsible for the HCO and NOR activities, to the best of our knowledge the difference of nonheme metal ion has not been addressed systematically.

To overcome the above limitations, our group has engineered sperm whale myoglobin into a structural and functional model of HCO (L29H, F43H, H64 Mb, called Cu_BMb), which was able to bind Cu and reduce O_2 to H_2O.[22–24] Further designs improved both the number of turnovers,[25] as well as the overall rate of O_2 reduction, even matching the activity observed in native systems.[26] However, Cu_BMb was unable to bind Fe, not surprisingly, as it lacks the conserved Glu in the Fe-binding site of NORs. Therefore, we added Val68Glu to Cu_BMb, which binds nonheme Fe and exhibits NOR activity, making this protein (called Fe_BMb, Figure 1a) a structural and functional model of NOR.[27–30] Given its ability to bind either Fe, Cu, or Zn in the nonheme metal binding site with almost identical geometric structures, this Fe_BMb became an excellent system to answer the question of the why HCO and NOR use their respective nonheme metal ion in their activities.[27,29,31,32] Our findings indicate that both nonheme Fe and Cu impart the full $4e^-$, $4H^+$ O_2-reduction activity to water in Fe_BMb, while redox-inactive Zn and Fe_BMb without nonheme metal are unable to effectively reduce O_2 without large generation of ROS.[13] More importantly, we found 30-fold and 11-fold enhancements in oxidase activity of Cu- and Fe-bound HCO mimics, respectively, as compared to Zn-bound mimics. Detailed electrochemical, kinetic and vibrational spectroscopic studies, in tandem with theoretical DFT calculations, demonstrate that the nonheme metal not only donates electrons to oxygen but also activates it for efficient O-O bond cleavage. Furthermore, the higher redox potential of copper and the enhanced weakening of O-O bond from the higher electron density in the d-orbital of copper are central to its higher oxidase activity over iron. This direct comparison of the effect of Cu and Fe in promoting O_2 reduction in the same protein scaffold with otherwise identical active site has allowed us to provide direct evidence for why nature prefers Cu over Fe in oxidase activity and reasons behind such a choice.

Built upon the above success in elucidating the role of nonheme Cu and Fe ion in HCO activity, we explored further if the nonheme metal ion can be replaced with other first-row transition metal ions such as Mn and Co with different d electron configurations and examined whether their presence imparted O_2 reduction activity. Cobalt and manganese have been used previously as robust probes to uncover necessary electronic structural properties and structure-activity relationships in other proteins.[33–36] including superoxide dismutase,[37–41] catechol dioxygenase,[42] myoglobin,[43,44] P_{1B}-type ATPases,[45] and metallothioneins.[46] Understanding the roles of nonheme metal ions beyond the Cu and Fe in native HCO and NOR will provide deeper insights into nature's choice of metal ion and allow finer control of the activity beyond native enzymes. Such an endeavor is a primary goal of protein design,[47,48] and, while oftentimes the metals within a designed protein are not viewed as equally 'mutatable' the same way an amino acid is, changes to these crucial cofactors provide valuable insights into the enzymatic structure-function relationship. Toward this goal, we report herein preparation and characterization of the binding of Mn and Co in the nonheme site of Fe_BMb. The results showed that, while both Co and Mn confer O_2 reduction to H_2O with high selectivity toward H_2O, the redox activity of Co and Mn is not

strictly required, in contrast to those observed for the Cu and Fe-dependent activity. Spectroscopic studies coupled with DFT calculations were carried out to explain mechanistic differences in these nonheme metal ion-dependent activities.

Materials and Methods

All chemicals and reagents were purchased from Sigma-Aldrich and used without additional purification. In this manuscript we will designate the corresponding metallated derivatives as M^{II}–Fe_BMb(Fe^{II}) where the M^{II} represents a metal ion with the designated oxidation state (II) occupies the nonheme Fe_B center and the Fe^{II} represents Fe^{II}-protoporphyrin IX (heme) in the heme-binding site. When the Fe_B center is empty, it will represented as E-Fe_BMb(Fe^{II}).

Expression, purification, and formation of nonheme-bound proteins

E-Fe_BMb(Fe^{III}) was expressed and purified as described previously, with small changes.[27,29] Proteins were expressed using *E. coli* BL21(DE3) Competent cells (New England Biolabs). Proteins were refolded through dialysis against 10 mM Tris at pH 8.0. After refolding, buffer exchange was achieved by loading onto a size exclusion column equilibrated with 100 mM potassium phosphate pH 7. After purification, Fe_BMb(Fe^{III}) was degassed using standard Schlenk line techniques, brought into a Coy Labs vinyl type anaerobic chamber (<1 ppm O_2), reduced using dithionite, and buffer exchanged using Sephadex G-25 PD-10 Desalting Columns (GE Life Sciences) equilibrated with 50 mM Bis-Tris pH 7.3. M^{II}-Fe_BMb(Fe^{II}) bound forms of the protein were obtained by addition of 2 molar equivalents metal (with respect to protein) to E-FeBMb(Fe^{II}), and any unbound M^{II} ions were removed by PD-10 column. The metal sources for Mn^{II} and Co^{II} were $MnCl_2 \cdot 6H_2O$ and $CoCl_2 \cdot 6H_2O$, respectively.

Crystallization of M^{II}-Fe_BMb(Fe^{II})

Crystals of Fe_BMb(Fe^{III}) were grown as previously described,[27] with slight changes. Crystals were grown aerobically in large (~150 – 200 μL) sitting drops of 1.5 mM protein solution in 20 mM potassium phosphate pH 7 mixed 1:1 with well buffer (0.2 M sodium acetate trihydrate, 0.1 M sodium 2-(N-morpholino)ethansulfonate (MES) pH 6.5 and 30% w/v PEG 10,000). This mixture was equilibrated via vapor diffusion against 30 mL of the crystallization solution at 4°C. Crystals appeared within 3 days and matured after 1 week. Nonheme metal-bound crystals were prepared by anaerobic soaking of ~10 eq. of the appropriate metal solution in a mixture of Fe_BMb(Fe^{II}) and well buffer. A cryoprotectant of 50% PEG 400 was used immediately prior to freezing the crystals using liquid nitrogen.

Data collection

Diffraction of Mn^{II}- and Co^{II}-Fe_BMb(Fe^{II}) was carried out at 100 K using beamline 14-1 at SSRL. Data were processed using the HKL2000 package.

Structure determination

These structures were solved via molecular replacement using the PHENIX software suite,[49] with PDB 3K9Z as a starting model. Multiple rounds of automated model building and

refinement using PHENIX, as well as manual model modification using Coot, were carried out to generate the final structures. PyMol was used to generate the figures shown. The structures were deposited to the PDB with accession codes 5VNU and 5VRT for Mn^{II}- and Co^{II}-Fe_BMb(Fe^{II}), respectively.

UV/Vis spectroscopy

Preparation of the nonheme metal-bound forms of Fe_BMb(Fe^{II}) inside of the anaerobic chamber utilized UV/Vis spectroscopy collected on a Hewlett-Packard 8453 spectrophotometer.

O_2 consumption assays

The rate of water and ROS production was measured and calculated previously reported.[13,25,50,51] Metal-bound protein variants were prepared and transferred outside to an Oxytherm Clark-Type electrode (Hansatech) using gas-tight syringes (Hamilton Co.). The reaction was started via addition of 18 μM protein to a solution containing 1.8 mM TMPD, 18 mM ascorbate, and air-saturated 100 mM potassium phosphate pH 6. Experiments were also carried out at 40 μM protein using O_2-saturated buffer at ~800 μM, in the same buffer using the same amount of TMPD and ascorbate. The ratio of ROS/water formation was determined by repeating the measurements in the same solution with 7 μM catalase and 250 U superoxide dismutase (SOD) added to selectively react with H_2O_2 and O_2^-, respectively, generating O_2. This leads to an apparent decrease in the O_2 consumption rate which can be used to compare the rates with and without catalase/SOD and to calculate the ratio of ROS/water formed.

Spectroelectrochemistry

The heme redox potential (E°) was determined using an optically transparent thin-layer cell and measured spectroelectrochemically via UV/Vis on a CARY 3E as described previously. Potential steps of 25 mV the range of −300 to +200 mV vs SHE were used. Global analysis of the data was done using SpecFit.[13,51]

Stopped-flow UV/Vis

Stopped flow measurements were done on an Applied Photophysics SX18.MV spectrometer with a 256-element photodiode array detector. Equal volumes of $M^{II-}Fe_B$Mb(Fe^{II}) and oxygen-saturated buffer solutions were mixed. The apparatus was equipped with a NESLAB RTE-111 refrigerated bath chiller circulator that was used to maintain the reaction temperature at 8°C. Logarithmic data sampling was used on a total of 1000 spectra collected over a 300 s timescale.

X-ray absorption near edge structure (XANES) measurements

XANES samples were prepared anerobically in custom-made 100 μL Lexan cells sealed with Kapton tape. All proteins were concentrated to ~2 mM before freezing. The 0 s timepoint samples were frozen in the XANES cells anerobically before exposure to O_2. 10 m timepoint samples were prepared by reacting the metal-added protein solution with O_2-saturated buffer before freezing. Mn- and Co-edge (6.537 and 7.709 keV, respectively) were

collected at the Stanford Synchrotron Radiation Lightsource (SSRL) operating at 3 GeV with 500 mA currents on beamline 9–3 using a Si monochromator (ϕ = 90°, energy cutoff 12 keV) and a Rh-coated mirror. Data were collected in fluorescence mode on a Canberra 100-element Ge array detector with maximum count rates below 120 kHz. Soller slits and a 3 μm Z-1 (Mn oxide) filter were placed between the samples and the detector array to reduce Compton and elastic scattering. Edge energy was calibrated against an Fe reference foil that was scanned simultaneously with every sample. Samples were scanned 4–6 times divided between 2–3 spots (2 mm × 3 mm) in the sample holder at a temperature of 8–10 K and averaged for analysis. XANES data were collected from ~150 eV above and below the edge energies of the specific metals being investigated to aid in background subtraction and normalization with energy steps of 0.25 eV in the edge region. Data analysis was performed using Athena from the Demeter software suite. A flat pre-edge was achieved by subtracting a line anchored through points at least 30 eV below the edge, and the spectra was normalized by subtracting a second order polynomial fixed to points greater than 60 eV above the edge.

Resonance Raman (RR) measurements

Rapid freeze quench (RFQ) was used to prepare O_2-reacted complexes of Mn^{II}- and Co^{II}-$Fe_BMb(Fe^{II})$ from the single millisecond to tens of second range, and followed a previously described protocol.[13,52] M^{II}-$Fe_BMb(Fe^{II})$ was prepared anaerobically as described above (Omnilab System, Vacuum Atmospheres Co.), then loaded into RFQ glass syringes. 7 mL of either $^{16}O_2$ or $^{18}O_2$ gas was added to 2.5 mL of degassed buffer in air-tight serum bottles, incubated for 1 hour, then loaded into RFQ glass syringes to prepare O_2-saturated buffers. The RFQ syringes were screwed into the System 1000 Chemical/Freeze Quench Apparatus (Update Instruments) and immersed in a water bath at 4 °C. Reactor length and displacement rate were adjusted accordingly for specific time points. For the millisecond time points, a total volume of ~250 μL of the solutions were rapidly mixed by the apparatus and frozen inside an NMR tube cooled to −120 °C using liquid ethane. Longer time points on the second scale were prepared and frozen manually using a similar setup. Resonance Raman was collected before and after ethane removal via 80°C incubation for 2 hours. Measurements were collected using a 407 nm excitation from a Kr laser (Innova 302C, Coherent) using a McPherson 2061/207 spectrograph equipped with a liquid nitrogen cooled CCD detector (LN-1100 PB, Princeton Instruments). A long pass filter (RazorEdge, Semrock) was used to attenuate Rayleigh scattering. Samples were kept at 110 K using liquid nitrogen. Sample photosensitivity was determined by short spectral acquisition with low laser power while spinning the sample and comparing the porphyrin skeletal modes in the high-frequency region. The frequencies were calibrated relative to aspirin and are accurate to ±1 cm^{-1}.

DFT calculations

All residues coordinated to Fe and Co/Mn are included in the calculations and truncated at Cα atoms. In Co^{II}-$Fe_BMb(Fe^{II})$, H43 is also included in the model because it is hydrogen bonded to a water molecule (W39) coordinated to Co. A non-substituted porphyrin (Por) was used in the models. All models were subject to partial geometry optimizations with only protein residue Cα atoms frozen at the X-ray structure positions to mimic the protein

environment based on previous work.[53] All calculations were performed using the Gaussian 09 program with the DFT method B3LYP[54] and the 6-311G(d) basis for all heavy atoms and 6-31G(d) for hydrogens, similar to previously reported related metalloprotein model studies.[55–57] The bulk protein environment was simulated with the self-consistent reaction filed method using the PCM approach with a dielectric constant of 4.0 as previously reported.[58] In addition to electronic energy E, the zero-point energy corrected electronic energy (E_{ZPE}), and the enthalpy (H) and Gibbs free energy (G) at ambient conditions were calculated in each case. The atomic charges using the Natural Population Analysis (NPA) and Muliken spin densities were also calculated. As shown in the Supporting Information, both ferromagnetically and anti-ferromagnetically coupled Fe and Mn/Co systems were studied and found to have insignificant difference in energies; thus, only the anti-ferromagnetically coupled Fe and Mn/Co systems were discussed here.

Results and Discussion

We first determined whether Mn^{II} or Co^{II} binds to E-Fe_BMb(Fe^{II}) using UV/Vis spectroscopy. UV/Vis spectroscopy is advantageous in studying E-Fe_BMb(Fe^{II}) in that nonheme metal binding close to the heme center can result in a shift of the heme spectrum, which provides a rapid and clear indication of nonheme metal binding.[3,27,29,30,59] Therefore, we titrated Mn^{II} to a solution of E-Fe_BMb(Fe^{II}), and observed a red shift of the Soret band from 433 nm to 434 nm, as well as a splitting of the 557 nm peak in the visible region of the spectrum, indicative of Mn^{II} binding to the nonheme metal site.[27,29,30] Similar spectral changes were observed upon addition of Co^{II} to E-Fe_BMb(Fe^{II}) (Figure S2). By measuring the spectral changes upon addition of sub-stoichiometric to excess (~5 eq.) amounts of nonheme metal, K_d values of 35 μM and 9 μM for Mn^{II} and Co^{II}, respectively, were obtained. Interestingly, the K_d of Fe^{II} binding to the nonheme site of E- Fe_BMb(Fe^{II}) was determined to be 22 μM,[30] and, when compared the affinities of these three metal ions for the designed nonheme site, follows the Irving-Williams series trend of $Mn^{II} < Fe^{II} < Co^{II}$

Having determined the affinity of metal binding at the nonheme site in E-Fe_BMb(Fe^{II}) using UV/Vis, we measured the rate of oxygen reduction quantitatively using an O_2 Clark-type electrode and a protocol reported previously in native HCO.[60–63] A critical factor in determining the success of Mn^{II}- and Co^{II}-Fe_BMb(Fe^{II}) as models of HCO is demonstrating that they are capable of the selective and complete 4-electron and 4-proton reduction of oxygen to water without the release of reactive oxygen species (ROS), such as peroxide or superoxide.[64–69] In order to determine the O_2 reduction product, we added superoxide dismutase (SOD) and catalase, which selectively react with superoxide and peroxide, respectively, forming O_2 and resulting in a decreased rate of O_2 consumption relative to the amount of ROS produced.

In all cases, an initial rapid drop in [O_2] was observed, attributable to O_2 binding to heme (Figure 2). In the absence of any metal ion in the nonheme site, O_2 reduction using 18 μM E-Fe_BMb(Fe^{II}) results in an initial rate of 0.21 ± 0.03 μM/s, with 73% ROS formation.[70] The presence of Mn^{II} and Co^{II} at the nonheme site in E-Fe_BMb(Fe^{II}) had two effects. First, both nonheme metals increase the rate of O_2 reduction compared to E-Fe_BMb(Fe^{II}) to 1.14 and 1.01 μM/s, respectively. Second, the presence of Mn^{II} and Co^{II} in the nonheme site

resulted in greatly reduced ROS generation, displaying only 7% and 1%, respectively. In comparison O_2 reduction by Fe^{II}-Fe_BMb(Fe^{II}) resulted in 4% ROS formation.[13] Control experiments using wild-type myoglobin in the presence of Mn^{II} and Co^{II} showed similar rates to E-Fe_BMb(Fe^{II}), as well as a large percentage of ROS production, > 75% (Figure S3), indicating that the designed mutations of Fe_BMb are responsible for binding of Mn^{II} and Co^{II} and for their respective activities. While the rates of O_2 reduction by Mn^{II}- and Co^{II}-Fe_BMb(Fe^{II}) are comparable to that of Fe^{II}-Fe_BMb(Fe^{II}) (1.15 μM/s), the percentages of ROS formation (7, 4 and 1%) for Mn^{II}, Fe^{II} and Co^{II} derivatives follow the same trend as that of metal binding affinities (35, 22 and 9 μM), suggesting that higher affinity for the metal ion is associated with lower percentage of ROS formation. Furthermore, another trend is also followed in the total turnover numbers (TTN), as higher affinity has resulted in higher TTN for Mn^{II}-, Fe^{II}-, and Co^{II}-Fe_BMb(Fe^{II}) completing 5.1 ± 1.1, 13.4 ± 0.7, and 82.5 ± 2.5 total turnovers, respectively (Figure S4). Since the above results were obtained using 18 μM of protein, we carried out additional experiments using 40 μM protein, conditions where the nonheme sites would have higher metal occupancy. Interestingly, the TTN for Mn^{II}-, Fe^{II}-, and Co^{II}-Fe_BMb(Fe^{II}) increased from 5.1 ± 1.1, 13.4 ± 0.7 and 82.5 ± 2.5, respectively, at 18 μM protein, to 11.0 ± 1.3, 17.8 ± 1.2, and 92.8 ± 7.4, respectively, at 40 μM protein, with %ROS decreasing from 7, 4, and 1%, to 5, 2.5, and 1%, respectively, at 40 μM protein (Figure S5). These results suggest that the higher metal occupancy of the nonheme site resulted in less pronounced differences in TTN and %ROS, but maintained the trend observed at the lower protein concentration.

In order to understand the interesting differences in O_2 reduction activity described in the above paragraph, we next carried out mechanistic investigations of the reaction. Our first step in this process was to determine if the redox activity of each nonheme metal ion plays any role in this reaction. In native HCO, the nonheme Cu^I has been shown to donate an electron during the O_2 reduction catalytic cycle.[69] However, results from synthetic models of the heme-copper center in HCO using small organic molecules as ligands suggest that the nonheme metal ion may act as a Lewis acid, and does not participate directly in electron donation.[71,72] Using the biosynthetic model of Fe^{II}- and Cu^I-Fe_BMb(Fe^{II}), we had previously reported that the propensity of Fe^{II} or Cu^I to donate electrons to heme-bound oxygen is responsible for the difference in O_2 reduction activity. Because Fe^{II} and Cu^I are very different, not only in charges but also in geometric properties, the above conclusion from biosynthetic modeling studies is tentative. Since Mn^{II} and Co^{II} have the same charge as Fe^{II}, with the major difference among the three metal ions being d electron configuration, studying Mn^{II}- and Co^{II}-Fe_BMb(Fe^{II}) and comparing them with Fe^{II}–Fe_BMb(Fe^{II}) offers a unique opportunity to elucidate the precise role of d electron-based redox in the O_2 reduction activity.

We used XANES spectroscopy to determine the redox state of the nonheme metal ion before and after reaction with O_2. Both the pre-edge and edge energies in the XANES spectrum of Mn^{II}-Fe_BMb(Fe^{II}) do not shift after reaction with O_2 (Figure 3). The overall shape and intensities of each spectrum are also similar, supporting the presence of Mn^{II} both before and after reaction with O_2.[73] For Co^{II}-Fe_BMb(Fe^{II}), prior to reaction with O_2, the edge energy is ~ 7718 eV. Upon reaction with O_2, the edge energy shifts ~4 eV to 7722 eV (Figure 3). Additional changes included a moderate attenuation of the pre-edge feature 7112

eV and increase in the main peak intensity at 7727 eV. Post edge features at 7740 eV, 7752 eV, and 7768 eV, showed slight changes in intensity as well. None of these features had an energy shift after reaction with O_2.

Previous reports of Co^{III} complexes typically have a main absorption peak at ~ 7730 eV, as well as a secondary peak near 7720 eV. Co^{II} complexes, on the other hand, possess a single peak at lower energy ~7720 eV.[74] Additionally, Co^{II} XANES in the post-edge region display a local minimum intensity ~ 7745 eV, which leads to a broad shoulder near 7760 eV. On the other hand, Co^{III} displays a peak ~ 7730 eV, which leads to a local minimum intensity ~ 7755 eV. Finally, previous studies of Co complexes report significant attenuation of white line intensity upon oxidation from Co^{II} to Co^{III}.[74] While the ~4 eV shift in the edge energy of Co^{II}-$Fe_BMb(Fe^{II})$ reacted with O_2 is notable, the overall shape and position of other features most closely resembles Co^{II} complexes. We attributes such small changes to geometry or the ligand set of the nonheme Co^{II} caused by reaction of O_2 with Co^{II}-$Fe_BMb(Fe^{II})$, and not from oxidation to Co^{III}. This conclusion is supported by the DFT optimized structures of the oxygen-bound form of the protein indicate a more octahedral geometry for Co^{II}, which our XANES data most closely match with (*vide infra*).[74] Overall, the XANES spectra for Co^{II}-$Fe_BMb(Fe^{II})$ are indicative of Co^{II} present at the nonheme site both before and after reaction with O_2.[74,75] In contrast, previous XANES studies showed both nonheme Cu^{I} and Fe^{II} were oxidized to Cu^{II} and Fe^{III} under similar conditions.[13] These results are interesting and indicate that, in contrast to Fe^{II}- and Cu^{I}–$Fe_BMb(Fe^{II})$, whose nonheme metals rapidly donate electrons to a heme-oxy species during the O_2 reduction reaction, we do not observe oxidation of Mn^{II} or Co^{II} during this same activity.

Since we did not observe oxidation of Mn^{II} or Co^{II} during the O_2 reduction reaction in M^{II}–$Fe_BMb(Fe^{II})$, we wondered whether they influence the activity by exerting an effect on the heme reduction potential. We utilized spectroelectrochemistry to measure the heme Fe^{III}/Fe^{II} reduction potential $E°'_{heme}$ in the presence of different nonheme metal ions. The $E°'_{heme}$ in E-$Fe_BMb(Fe^{II})$ was determined to be −158 ± 4 mV, and increased to 23 ± 4 mV and 4 ± 1 mV upon binding of Mn^{II} and Co^{II}, respectively (Figure S6). Similar trends in the $E°'_{heme}$ were observed upon binding of Fe^{II}, Cu^{I}, and Zn^{II}, with values of −46 ± 4 mV, −64 ± 4 mV, and −45 ± 2 mV, respectively.[13,27] Given the similar shift in $E°'_{heme}$ across all nonheme metal ions added, even though some displayed very different O_2 reduction activity, we concluded that the influence of the nonheme metal ions on the $E°'_{heme}$ does not play a role in the different O_2 reduction activities.

We next probed the interaction of O_2 with Mn^{II}- and Co^{II}-$Fe_BMb(Fe^{II})$ using stopped flow UV/Vis spectroscopy. Mn^{II}-$Fe_BMb(Fe^{II})$ very rapidly forms a transient spectrum with visible peaks at 547 and 577 nm characteristic of heme-oxy complexes,[50,76–78] which then converts to Mn^{II}–$Fe_BMb(Fe^{III})$. Co^{II}-$Fe_BMb(Fe^{II})$ formed a spectrum with peaks in the visible region at 544 and 583 nm (Figure 4A, blue), also characteristic of oxygen-bound heme,[50,76–78] that transitions to a spectrum resembling Co^{II}-$Fe_BMb(Fe^{III})$ with visible peaks at 498 and 619 nm (Figure 4A). The transitions of Mn^{II}- and Co^{II}-$Fe_BMb(Fe^{II}$-$O_2)$ to Mn^{II}- and Co^{II}-$Fe_BMb(Fe^{III})$ proceed with isosbestic points at approximately 520 nm for both variants, and 599 nm for the Co^{II} variant only, indicating no observation of additional intermediate formation, likely due to the lack of electron donation from the nonheme metals,

after oxygen binds to heme, supporting the conclusions drawn from the XANES data, above. Compared to Mn^{II}-Fe_BMb(Fe^{II}), however, Co^{II}-Fe_BMb(Fe^{II}) formed the heme-oxy species more slowly (k_{obs} = 41.2 s^{-1} and 2.64 s^{-1}, respectively) and was slower to decay to M^{II}-Fe_BMb(Fe^{III}), (k_{obs} = 0.971 and 0.119 s^{-1}, respectively). Higher-order iron-oxo species, such as Fe^{IV}=O which is implicated in the HCO mechanism,[79] and other similar species were not observed in these case.[80,81] Interestingly, a clear formation of heme-oxy was not observed in Fe^{II}- or Cu^{I}-Fe_BMb(Fe^{II}) because the nonheme Fe^{II} or Cu^{I} donates an electron to heme-bound oxygen.[13] This electron transfer thus leads to more highly reactive heme-oxygen species, such as peroxy which were unable to be detected.[13] On the other hand, when redox inactive Zn^{II} is bound at the nonheme site a stabilized heme-oxy complex is observed, due to lack of electron donation from the nonheme metal.[13] The similarities between the spectra of Mn^{II}-,Co^{II}-, and Zn^{II}-Fe_BMb(Fe^{II}) upon reaction with O_2-saturated buffer suggest that these nonheme metals do not donate electrons during this reaction. Ultimately, the formation of the more stabilized reaction intermediate in Co^{II}-Fe_BMb(Fe^{II}) could help to explain why this derivative has the smallest % ROS production and highest turnover observed in comparison with Mn^{II}- and Fe^{II}-Fe_BMb(Fe^{II}), given that release of ROS will lead to self-degradation of the enzyme.[82,83]

Intrigued by these results, we next investigated the same reaction in the presence of excess (~100/1000 eq.) TMPD/ascorbate, acting as electron donor and sacrificial reductant, respectively, simulating multi-turnover conditions. For Mn^{II}-Fe_BMb(Fe^{II}), the spectrum rapidly converted from the starting Mn^{II}-Fe_BMb(Fe^{II}) to a heme-oxy like spectrum with peaks at 547 and 577 nm, and then continues to react forming ferric Mn^{II-}FeBMb(Fe^{III}), similar to the case without TMPD/Ascorbate present. Similarly, Co^{II}-Fe_BMb(Fe^{II}) formed peaks at 544 and 583 nm (Figure S7), consistent with heme-oxy formation and, again, similar to the single-turnover conditions. Under multi-turnover conditions, however, Co^{II}-Fe_BMb(Fe^{II}-O_2) then transitioned to steady state, displaying peaks at 498, 544, 583, and 619nm, which is indicative of a mixture of the ferric product and oxy-heme intermediate. Upon consumption of O_2, the spectrum returns to ferrous heme, with visible peaks at 551 and 573nm, as well as a small shoulder near 514 nm, suggesting that nonheme Co^{II} still bound to the nonheme site of Fe_BMb,[27,29–32] which is critical for additional rounds of catalysis. This key difference in reactivity further helps to highlight the differences in total turnover between Mn^{II}- and Co^{II}-Fe_BMb(Fe^{II}) towards O_2 reduction, and to showcase the importance of nonheme metal ion identity in maintaining O_2 reduction activity by forming stable intermediates during the reaction.

Having identified a heme-oxy species in both Mn^{II}- and Co^{II}-Fe_BMb(Fe^{II}), we investigated the impact that these nonheme metals had on the heme-oxy O-O bond length, and their effect on oxygen activation, using resonance Raman (RR) spectroscopy. Rapid freeze quench (RFQ) samples were prepared with $^{16}O_2$ and $^{18}O_2$-saturated buffer. The high-frequency RR spectra show that optimum enrichment for a heme-oxy complex (ν_4 at 1377 cm^{-1}) relative to the starting ferrous and ending ferric products (ν_4 at 1353 and 1371 cm^{-1}, respectively) (Figure 5). Low frequency RR spectra were used to characterize the $\nu(Fe_{heme}$-$O_2)$ modes (Figure S8). For Co^{II}-Fe_BMb(Fe^{II}-O_2), $\nu(Fe_{heme}$-$O_2)$ was detected at 599 cm^{-1}, which is similar to that observed in Zn^{II}-Fe_BMb(Fe^{II}-O_2) and is indicative of a strengthening of the Fe-O bond, but a weakening of the O- O bond. These data are consistent with our

previous determination that the nonheme metal ion is capable of activating heme-bound oxygen. Taken together with the XANES data of Co^{II}–Fe_BMb(Fe^{II}) reaction with O_2, evidence suggests that nonheme Co^{II} does not donate electrons during the reduction of O_2, but is still capable of activating the O-O bond for efficient reduction to H_2O. Therefore, in the case of O_2 reduction using binuclear heterometallic heme-nonheme systems, we do not observe electron donation from certain nonheme metals for efficient 4-electron reduction of oxygen to water. It appears that this reduction activity can still be accomplished through O-O bond activation by the nonheme metal, perhaps acting as a Lewis acid and not a redox partner, as described previously for synthetic systems.[71,72] The Lewis acidity of other divalent metal ions, such as Mg^{II}, Ca^{II}, Sr^{II}, and Ba^{II}, was previously quantified from the g_{ZZ} values of the EPR spectra of [M]-O_2^- complexes, and in the cases where oxidation state was the same, metal Lewis acidity would increase with decreasing ionic radii.[84] The ionic radii trend for the nonheme metals investigated here is Mn^{II} (0.83 Å) > Fe^{II} (0.78 Å) > Co^{II} (0.75 Å).[85] Co^{II}, being the metal with the smallest radii, would thus be the strongest Lewis acid among the three. While we state that the O_2 reduction rate is similar for the different nonheme metal variants at 18μM, the %ROS formation follows the trend Mn^{II} > Fe^{II} > Co^{II}. Thus, it appears that the stronger the Lewis acidity, the more heme-bound oxygen is activated, allowing for easier cleavage of the O-O bond to produce more water in the case of these three metal ions.

To understand structural features responsible for the differences in binding affinities and reactivity among the three metal ions, we employed x- ray crystallography to determine the binding site of Mn^{II} and Co^{II} in Fe_BMb(Fe^{II}). Diffraction data of Mn^{II}- and Co^{II}-Fe_BMb(Fe^{II}) at 1.5 Å and 1.9 Å, respectively, were collected above and below the K-edge for the respective metal, confirming that each crystal structure contained the specific nonheme metal ion in the designed nonheme site in the distal heme pocket of Fe_BMb(Fe^{II}) (Figure 1A). As a point of reference, Fe^{II} is the metal cofactor in the original design of nonheme site, and was shown by crystallography to contain Fe_B coordinated by imidazole nitrogens of H29, H43, and H64, OE1 of E68 and a water molecule. The bond distances between Fe_B and OE1 and OE2 of E68 are 2.19 Å and 3.28 Å, respectively, indicating that the E68 coordinated to Fe monodentantly. When Mn^{II} is bound at the nonheme site, its overall coordination sphere and geometry is similar to that of Fe^{II} (Table 1), but some of the bond lengths have been extended, likely leading to the weaker K_d determined for Mn^{II} binding compared to Fe^{II}. When Co^{II} is bound in the nonheme site, the nitrogens of both H29 and H64 coordinate to Co^{II} directly, like in Fe^{II}- and Mn^{II}-Fe_BMb(Fe^{II}), but H43 does not. Instead, it is replaced by a water molecule that is coordinated to the Co^{II} at a distance of 2.34 Å while hydrogen-bonding to one of the nitrogens of H43 at a distance of 2.38 Å. In addition, the distances between the Co^{II} and OE1 and OE2 of E68 are 2.36 Å and 2.12 Å, respectively, suggesting that E68 coordinates to Co^{II} bidentantly. Finally, there is another water molecule at a similar position as the water in Fe^{II}- and Mn^{II}–Fe_BMb(Fe^{II}), making Co^{II} coordination sphere a near-octahedral geometry. Petrik et. al. recently identified the role that an extended hydrogen bonding network plays in promoting O_2 reduction activity in a similar model protein to those used in this study.[86] Specifically, introduction of an extended hydrogen-bonding network allowed for efficient proton delivery necessary for the designed O_2 reduction activity through formation of more appropriate intermediates compared to the

wild type protein. Similarly, the presence of an additional water molecule in the $Co^{II-}Fe_BMb(Fe^{II})$ structure compared to the Mn^{II} and Fe^{II} forms could promote a similar effect through enhanced proton shuttling leading to O-O bond cleavage.

These structural differences and bonding interactions are a likely cause for the observed stronger binding of Co^{II} compared to both Mn^{II} and Fe^{II}, which in turn leads to the higher total turnovers of Co^{II}-$Fe_BMb(Fe^{II})$. Additionally, with respective to heme ligation and coordination, there are important differences. The bond length between O1 of E68 and heme iron is 3.44, 3.22, and 2.46 Å for Fe^{II}-, Mn^{II}-, and Co^{II}-$Fe_BMb(Fe^{II})$, respectively. Thus, O1 of E68 in $Co^{II-}Fe_BMb(Fe^{II})$ coordinates heme iron, as opposed to the other cases. Such a crowded environment with Co^{II} present is likely a key factor for the rate at which the heme-oxy spectrum is formed in these variants, with Mn^{II}-$Fe_BMb(Fe^{II})$ forming heme-oxy much more rapidly (*vide supra*) given the less crowded heme site.

To help understand the oxy intermediates, and the role nonheme metal is playing in terms of oxygen activation and redox activity, we employed density functional theory calculations. All residues coordinated to Mn^{II}- and Co^{II}-Fe_BMb are included in the calculations and truncated at Cα atoms, and modelled to match each respective crystal structure. O_2 was then added to the models, which were then energy-optimized.

As shown in Figure 6, O_2 can stably bind with both the heme iron and nonheme metal. Interestingly, regarding the oxy-bound forms for these two protein systems, even with initial setups of oxidized Mn^{III} and Co^{III} states, computational results show that the most favorable oxidation states for both Mn and Co remain +2, and thus strongly support the above experimental results indicating that these metals are not oxidized. Although these two metals do not provide electrons like in the case of Fe^{II} and Cu^{I} studied previously,[13] they do help activate O_2 as evidenced by elongated O-O bond lengths by ~0.03 Å compared to the empty nonheme site (Table 2). This is also in good agreement with resonance Raman experimental results. It is interesting to note that, in this oxy-bound form, although the Fe-O bond lengths for Mn^{II} and Co^{II}-$Fe_BMb(Fe^{II}$-$O_2)$ are similar (1.883 and 1.894 Å, respectively), the Co-O distance is significantly shorter than the Mn-O distance by 0.274 Å. This observation suggests that the positively charged metal center may have stronger interaction with the negatively charged O_2 moiety in the case of Co^{II} than Mn^{II} which helps stabilize the oxy-form. Indeed, the calculated Gibbs free binding energy of O_2 to this active site is −15.71 kcal/mol for Co^{II}-$Fe_BMb(Fe^{II}$-$O_2)$, which is much stronger than that for Mn, −1.43 kcal/mol. This is in excellent agreement with above observed slower decay rate of this oxy species in the case of Co^{II} vs. Mn^{II}. In addition, computational geometry optimization results of the O_2-free active sites also reproduced the x-ray structural features, supporting a key difference between Mn^{II} and Co^{II} in such structures: for Mn, there is a vacant coordination site above the heme plane available for incoming O_2, while for Co, that site is occupied by E68. Therefore, the O_2 binding to heme Fe in Co^{II}-$Fe_BMb(Fe^{II})$ needs to displace E68 coordination first, which takes more energy and slows down the process, consistent with experimentally observed slower formation rate of the oxy species than $Mn^{II-}Fe_BMb(Fe^{II})$. The DFT calculations also help to provide additional insights into the observed changes in the XANES spectra (*vide supra*) upon reaction with O_2. Heme-bound O_2 in Mn^{II}- and Co^{II}-$Fe_BMb(Fe^{II})$ interacts more weakly with nonheme Mn^{II} than Co^{II}

(R_{M-O} of 2.400 and 2.126 Å, respectively) (Table 2), which would help explain the larger changes observed in the XANES spectra of Co^{II}-Fe_BMb(Fe^{II}) compared to Mn^{II}-Fe_BMb(Fe^{II}) when both are reacted with O_2. Additionally, O_2 replaces one of the Co^{II} Glu68 O ligands, forming a more octahedral geometry than the starting structure, which would lead to a XANES spectrum closely matching octahedral Co^{II}. Additional discussions regarding centrosymmetry of the Co^{II} center can be found in the supporting information. In the case of Mn^{II}-Fe_BMb(Fe^{II}), addition of O_2 to the DFT optimized structure leads most notably to a translation of the Mn^{II} and associated ligands more directly over the heme. The overall geometry of Mn^{II}, however, is largely maintained (Figure S9). These effects would help explain the smaller changes in the XANES spectra of Mn^{II}-FeBMb(Fe^{II}) when compared to Co^{II}-Fe_BMb(Fe^{II}).

Conclusion

In conclusion, we have investigated the roles of Mn^{II} and Co^{II} in conferring and fine-tuning O_2 reduction activity in a biosynthetic model of HCO/NOR in myoglobin. The Mn^{II} and Co^{II} binding at the nonheme iron site was observed with UV/Vis spectroscopy and confirmed by x-ray crystallography. Enzymatic activity assays of O_2 reduction with and without catalase and superoxide dismutase identified the majority of product formation as H_2O rather than ROS such as peroxide. Interestingly, the total turnover number and ROS production of each nonheme variant follows the same trend as K_d, suggesting that nonheme binding affinity plays an important role in the ability of each variant to perform multiple, complete reactions, especially given that E-Fe_BMb(Fe^{II}) displays poor O_2 reduction activity and product selectivity. Spectroscopic results from XANES and RR suggest that electron transfer from the nonheme metal ion is not *strictly* required for selective 4-proton, 4-electron reduction of O_2 to H_2O. Rapid stopped-flow UV/Vis and RR spectroscopies, coupled with DFT calculations, identified important mechanistic information regarding the roles of nonheme Mn^{II} and Co^{II} on O_2 binding and activation. Overall, our results clarify future efforts towards understanding specific structural, redox, and electronic features required for efficient O_2 reduction and may assist in future designs of catalysts for oxygen reduction for fuel cells.

Supplementary Material

Refer to Web version on PubMed Central for supplementary material.

Acknowledgments

The authors thank Daniel G. Nocera for helpful discussions and comments. We also thank P. Hosseinzadeh for experimental assistance involving data collection and analysis. J. R. was supported by a predoctoral training fellowship 5T32-GM070421 from the US National Institute of Health (NIH). E. M. was supported by a predoctoral training fellowship 5T32-GM8276-24 from the NIH. This material was supported in part by the US NIH under Award NIH R01GM062211 (to Y.L) and NIH R01GM074785 (to P.M.-L.) and by a US National Science Foundation (NSF) Award (NSF CHE-1300912 to Y.Z). Use of the Stanford Synchrotron Radiation Lightsource (SSRL), SLAC National Accelerator Laboratory, is supported by the US Department of Energy, Office of Science, Office of Basic Energy Sciences under contract # DE-AC02-76SF00515. The SSRL Structural Molecular Biology Program is supported by the Department of Energy Office of Biological and Environmental Research, and by the NIH National Institute of General Medical Sciences (NIHMS).

References

1. Buschmann S, Warkentin E, Xie H, Langer JD, Ermler U, Michel H. Science. 2010; 329:327–330. [PubMed: 20576851]
2. von Ballmoos C, Gennis RB, Ädelroth P, Brzezinski P. Proc Natl Acad Sci U S A. 2011; 108:11057–11062. [PubMed: 21690359]
3. Chakraborty S, Reed J, Sage JT, Branagan NC, Petrik ID, Miner KD, Hu MY, Zhao J, Alp EE, Lu Y. Inorg Chem. 2015; 54:9317–9329. [PubMed: 26274098]
4. Girsch P, de Vries S. Biochim Biophys Acta. 1997; 1318:202–216. [PubMed: 9030265]
5. Zhuang J, Amoroso JH, Kinloch R, Dawson JH, Baldwin MJ, Gibney BR. Inorg Chem. 2006; 45:4685–4694. [PubMed: 16749832]
6. Zhuang J, Reddi AR, Wang Z, Khodaverdian B, Hegg EL, Gibney BR. Biochemistry. 2006; 45:12530–12538. [PubMed: 17029408]
7. Van Wonderen JH, Oganesyan VS, Watmough NJ, Richardson DJ, Thomson AJ, Cheesman MR. Biochem J. 2013; 451:389–394. [PubMed: 23421449]
8. Duarte AG, Cordas CM, Moura JJG, Moura I. Biochim Biophys Acta BBA - Bioenerg. 2014; 1837:375–384.
9. Fujiwara T, Fukumori Y. J Bacteriol. 1996; 178:1866–1871. [PubMed: 8606159]
10. Forte E, Urbani A, Saraste M, Sarti P, Brunori M, Giuffrè A. Eur J Biochem. 2001; 268:6486–6491. [PubMed: 11737203]
11. Hayashi T, Lin I-J, Chen Y, Fee JA, Moënne-Loccoz P. J Am Chem Soc. 2007; 129:14952–14958. [PubMed: 17997553]
12. Collman JP, Dey A, Yang Y, Ghosh S, Decréau RA. Proc Natl Acad Sci. 2009; 106:10528–10533. [PubMed: 19541624]
13. Bhagi-Damodaran A, Michael MA, Zhu Q, Reed J, Sandoval BA, Mirts EN, Chakraborty S, Moënne-Loccoz P, Zhang Y, Lu Y. Nat Chem. 2017; 9:257–263. [PubMed: 28221360]
14. Lee SC, Holm RH. J Am Chem Soc. 1993; 115:11789–11798.
15. Collman JP, Fu L, Herrmann PC, Zhang X. Science. 1997; 275:949–951. [PubMed: 9020071]
16. Kim E, Helton ME, Wasser IM, Karlin KD, Lu S, Huang H, Moënne-Loccoz P, Incarvito CD, Rheingold AL, Honecker M, Kaderli S, Zuberbühler AD. Proc Natl Acad Sci. 2003; 100:3623–3628. [PubMed: 12655050]
17. Collman JP, Yang Y, Dey A, Decréau RA, Ghosh S, Ohta T, Solomon EI. Proc Natl Acad Sci. 2008; 105:15660–15665. [PubMed: 18838684]
18. Karlin KD, Fox S, Nanthakumar A, Murthy NN, Wei N, Obias HV, Martens CF. Pure Appl Chem. 2009; 67:289–296.
19. Schopfer MP, Wang J, Karlin KD. Inorg Chem. 2010; 49:6267–6282. [PubMed: 20666386]
20. Berto TC, Hoffman MB, Murata Y, Landenberger KB, Alp EE, Zhao J, Lehnert N. J Am Chem Soc. 2011; 133:16714–16717. [PubMed: 21630658]
21. Lehnert, N., Scheidt, WR., Wolf, MW. Structure and Bonding. Springer; Berlin Heidelberg: 2013. p. 1-69.
22. Sigman JA, Kwok BC, Lu Y. J Am Chem Soc. 2000; 122:8192–8196.
23. Sigman JA, Kim HK, Zhao X, Carey JR, Lu Y. Proc Natl Acad Sci. 2003; 100:3629–3634. [PubMed: 12655052]
24. Zhao X, Yeung N, Wang Z, Guo Z, Lu Y. Biochemistry. 2005; 44:1210–1214. [PubMed: 15667214]
25. Miner KD, Mukherjee A, Gao Y-G, Null EL, Petrik ID, Zhao X, Yeung N, Robinson H, Lu Y. Angew Chem Int Ed. 2012; 51:5589–5592.
26. Yu Y, Cui C, Liu X, Petrik ID, Wang J, Lu Y. J Am Chem Soc. 2015; 137:11570–11573. [PubMed: 26318313]
27. Yeung N, Lin Y-W, Gao Y-G, Zhao X, Russell BS, Lei L, Miner KD, Robinson H, Lu Y. Nature. 2009; 462:1079–1082. [PubMed: 19940850]
28. Lu Y, Yeung N, Sieracki N, Marshall NM. Nature. 2009; 460:855–862. [PubMed: 19675646]

29. Lin Y-W, Yeung N, Gao Y-G, Miner KD, Tian S, Robinson H, Lu Y. Proc Natl Acad Sci. 2010; 107:8581–8586. [PubMed: 20421510]
30. Chakraborty S, Reed J, Ross M, Nilges MJ, Petrik ID, Ghosh S, Hammes-Schiffer S, Sage JT, Zhang Y, Schulz CE, Lu Y. Angew Chem Int Ed. 2014; 53:2417–2421.
31. Hayashi T, Miner KD, Yeung N, Lin Y-W, Lu Y, Moënne-Loccoz P. Biochemistry. 2011; 50:5939–5947. [PubMed: 21634416]
32. Matsumura H, Hayashi T, Chakraborty S, Lu Y, Moënne-Loccoz P. J Am Chem Soc. 2014; 136:2420–2431. [PubMed: 24432820]
33. Bertini I, Canti G, Luchinat C, Mani F. J Am Chem Soc. 1981; 103:7784–7788.
34. Bertini I, Luchinat C. Adv Inorg Biochem. 1984; 6:71–111. [PubMed: 6442958]
35. Maret W, Vallee BL. Methods Enzymol. 1993; 226:52–71. [PubMed: 8277880]
36. Salgado J, Jiménez HR, Donaire A, Moratal JM. Eur J Biochem. 1995; 231:358–369. [PubMed: 7635147]
37. Bertini I, Lanini G, Luchinat C, Messori L, Monnanni R, Scozzafava A. J Am Chem Soc. 1985; 107:4391–4396.
38. Bertini, I., Manganl, S., Viezzoli, MS. Advances in Inorganic Chemistry. Sykes, AG., editor. Vol. 45. Academic Press; New York: 1998. p. 127-250.
39. Valentine JS, Doucette PA, Zittin Potter S. Annu Rev Biochem. 2005; 74:563–593. [PubMed: 15952898]
40. Ming L-J, Valentine JS. JBIC J Biol Inorg Chem. 2014; 19:647–657. [PubMed: 24692094]
41. Garcia YM, Barwinska-Sendra A, Tarrant E, Skaar EP, Waldron KJ, Kehl-Fie TE. PLOS Pathog. 2017; 13:e1006125. [PubMed: 28103306]
42. Fielding AJ, Lipscomb JD, L Q Jr. JBIC J Biol Inorg Chem. 2014; 19:491–504. [PubMed: 24615282]
43. Zahran ZN, Chooback L, Copeland DM, West AH, Richter-Addo GB. J Inorg Biochem. 2008; 102:216–233. [PubMed: 17905436]
44. Heinecke JL, Yi J, Pereira JCM, Richter-Addo GB, Ford PC. J Inorg Biochem. 2012; 107:47–53. [PubMed: 22178665]
45. Smith AT, Ross MO, Hoffman BM, Rosenzweig AC. Biochemistry. 2017; 56:85–95. [PubMed: 28001366]
46. Vašák, M. Methods in Enzymology. Riordan, James F., BLV, editor. Vol. 205. Academic Press; New York: 1991. p. 452-458.Metallobiochemistry Part B Metallothionein and Related Molecules
47. Maeda Y, Makhlynets OV, Matsui H, Korendovych IV. Annu Rev Biomed Eng. 2016; 18:311–328. [PubMed: 27022702]
48. Plegaria JS, Pecoraro VL. Methods Mol Biol Clifton NJ. 2016; 1414:187–196.
49. Adams PD, Afonine PV, Bunkóczi G, Chen VB, Davis IW, Echols N, Headd JJ, Hung L-W, Kapral GJ, Grosse-Kunstleve RW, McCoy AJ, Moriarty NW, Oeffner R, Read RJ, Richardson DC, Richardson JS, Terwilliger TC, Zwart PH. Acta Crystallogr D Biol Crystallogr. 2010; 66:213–221. [PubMed: 20124702]
50. Ibrahim M, Denisov IG, Makris TM, Kincaid JR, Sligar SG. J Am Chem Soc. 2003; 125:13714–13718. [PubMed: 14599210]
51. Bhagi-Damodaran A, Petrik ID, Marshall NM, Robinson H, Lu Y. J Am Chem Soc. 2014; 136:11882–11885. [PubMed: 25076049]
52. Matsumura H, Moënne-Loccoz P. Methods Mol Biol Clifton NJ. 2014; 1122:107–123.
53. Yang L, Ling Y, Zhang Y. J Am Chem Soc. 2011; 133:13814–13817. [PubMed: 21834502]
54. Becke AD. J Chem Phys. 1993; 98:5648–5652.
55. Zhang Y, Oldfield E. J Am Chem Soc. 2004; 126:9494–9495. [PubMed: 15291525]
56. Zhang Y, Oldfield E. J Am Chem Soc. 2008; 130:3814–3823. [PubMed: 18314973]
57. Ling Y, Zhang Y. J Am Chem Soc. 2009; 131:6386–6388. [PubMed: 19415933]
58. Torres RA, Lovell T, Noodleman L, Case DA. J Am Chem Soc. 2003; 125:1923–1936. [PubMed: 12580620]

59. Lin Y-W, Yeung N, Gao Y-G, Miner KD, Lei L, Robinson H, Lu Y. J Am Chem Soc. 2010; 132:9970–9972. [PubMed: 20586490]
60. Pawate AS, Morgan J, Namslauer A, Mills D, Brzezinski P, Ferguson-Miller S, Gennis RB. Biochemistry. 2002; 41:13417–13423. [PubMed: 12416987]
61. Brzezinski P, Gennis RB. J Bioenerg Biomembr. 2008; 40:521–531. [PubMed: 18975062]
62. Aoyama H, Muramoto K, Shinzawa-Itoh K, Hirata K, Yamashita E, Tsukihara T, Ogura T, Yoshikawa S. Proc Natl Acad Sci U S A. 2009; 106:2165–2169. [PubMed: 19164527]
63. Egawa T, Lee HJ, Gennis RB, Yeh S-R, Rousseau DL. Biochim Biophys Acta BBA - Bioenerg. 2009; 1787:1272–1275.
64. Babcock GT, Wikström M. Nature. 1992; 356:301–309. [PubMed: 1312679]
65. Ferguson-Miller S, Babcock GT. Chem Rev. 1996; 96:2889–2908. [PubMed: 11848844]
66. Michel H, Behr J, Harrenga A, Kannt A. Annu Rev Biophys Biomol Struct. 1998; 27:329–356. [PubMed: 9646871]
67. Wikström M. Biochim Biophys Acta. 2000; 1458:188–198. [PubMed: 10812033]
68. Brzezinski P, Larsson G. Biochim Biophys Acta. 2003; 1605:1–13. [PubMed: 12907296]
69. Yoshikawa S, Shimada A. Chem Rev. 2015; 115:1936–1989. [PubMed: 25603498]
70. Brantley RE, Smerdon SJ, Wilkinson AJ, Singleton EW, Olson JS. J Biol Chem. 1993; 268:6995–7010. [PubMed: 8463233]
71. Guilard R, Brandes S, Tardieux C, Tabard A, L'Her M, Miry C, Gouerec P, Knop Y, Collman JP. J Am Chem Soc. 1995; 117:11721–11729.
72. Chang CJ, Loh Z-H, Shi C, Anson FC, Nocera DG. J Am Chem Soc. 2004; 126:10013–10020. [PubMed: 15303875]
73. Chalmin E, Farges F, Brown GE. Contrib Mineral Petrol. 2009; 157:111–126.
74. Hall MD, Underwood CK, Failes TW, Foran GJ, Hambley TW. Aust J Chem. 2007; 60:180–183.
75. Bonnitcha PD, Hall MD, Underwood CK, Foran GJ, Zhang M, Beale PJ, Hambley TW. J Inorg Biochem. 2006; 100:963–971. [PubMed: 16624414]
76. Chen H, Ikeda-Saito M, Shaik S. J Am Chem Soc. 2008; 130:14778–14790. [PubMed: 18847206]
77. Unno M, Chen H, Kusama S, Shaik S, Ikeda-Saito M. J Am Chem Soc. 2007; 129:13394–13395. [PubMed: 17929929]
78. Garcia-Serres R, Davydov RM, Matsui T, Ikeda-Saito M, Hoffman BM, Huynh BH. J Am Chem Soc. 2007; 129:1402–1412. [PubMed: 17263425]
79. Wikström M, Verkhovsky MI. Biochim Biophys Acta BBA - Bioenerg. 2007; 1767:1200–1214.
80. Kwon H, Basran J, Casadei CM, Fielding AJ, Schrader TE, Ostermann A, Devos JM, Aller P, Blakeley MP, Moody PCE, Raven EL. Nat Commun. 2016; 7:13445. [PubMed: 27897163]
81. Nnamchi CI, Parkin G, Efimov I, Basran J, Kwon H, Svistunenko DA, Agirre J, Okolo BN, Moneke A, Nwanguma BC, Moody PCE, Raven EL. J Biol Inorg Chem. 2016; 21:63–70. [PubMed: 26666777]
82. Matsui T, Iwasaki M, Sugiyama R, Unno M, Ikeda-Saito M. Inorg Chem. 2010; 49:3602–3609. [PubMed: 20380462]
83. Kitatsuji C, Izumi K, Nambu S, Kurogochi M, Uchida T, Nishimura S, Iwai K, O'Brian MR, Ikeda-Saito M, Ishimori K. Sci Rep. 2016; 6:18703. [PubMed: 26729068]
84. Fukuzumi S, Ohkubo K. Chem – Eur J. 2000; 6:4532–4535. [PubMed: 11192086]
85. Shannon RD. Acta Crystallogr A. 1976; 32:751–767.
86. Petrik ID, Davydov R, Ross M, Zhao X, Hoffman B, Lu Y. J Am Chem Soc. 2016; 138:1134–1137. [PubMed: 26716352]

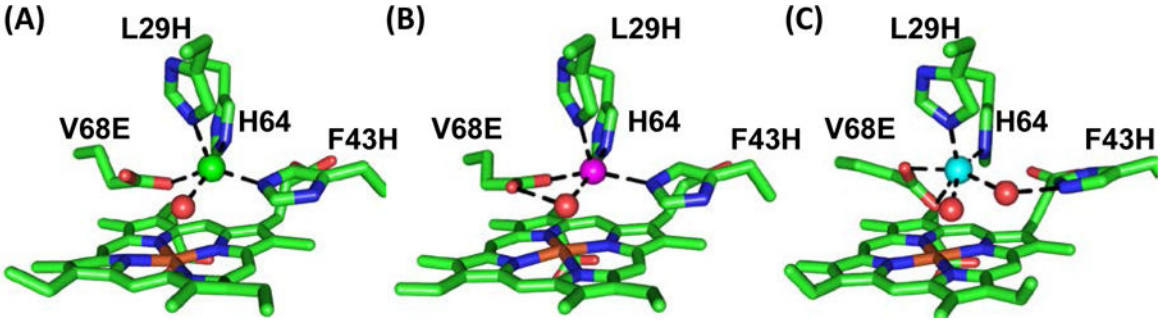

Figure 1.

Crystal structures of (A) Fe^{II}-, (B) Mn^{II}-, and (C) Co^{II}-FeBMb(Fe^{II}). Water molecules are shown as red spheres, while nonheme metal ions are shown as magenta, green, and cyan spheres for Mn^{II}, Fe^{II} and Co^{II}, respectively.

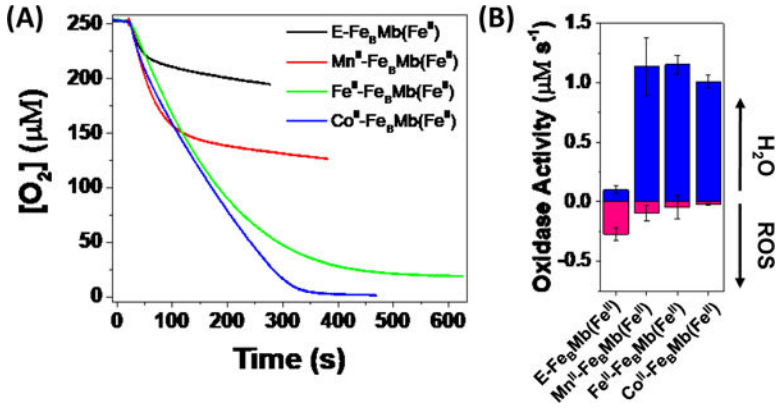

Figure 2.

(A) O_2 consumption traces of E-FeBMb(Fe^{II}) (black), Mn^{II}–FeBMb(Fe^{II}) (red), Fe^{II}-FeBMb(Fe^{II}) (green), and Co^{II}-FeBMb(Fe^{II}) (blue). (B) Oxygen consumption rates for all four nonheme metal protein variants.

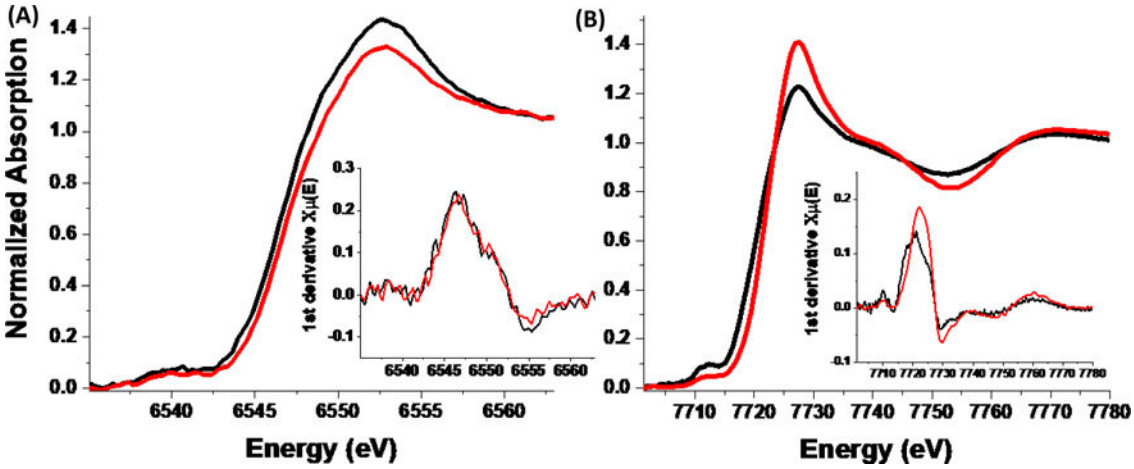

Figure 3.

XANES spectra of the reaction of (A) Mn^{II}-FeBMb(Fe^{II}) and (B) Co^{II}-FeBMb(Fe^{II}) with O_2-saturated 100 mM potassium phosphate pH 6. Black lines for each plot represent the protein before reaction with O_2, while red lines represent the protein 10 minutes after reaction with O_2. Insets show first derivative spectra.

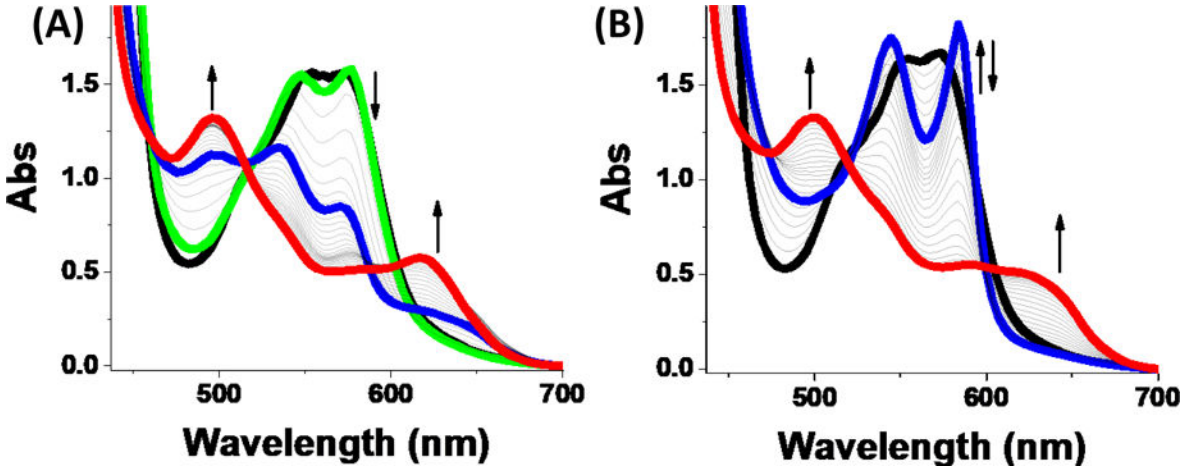

Figure 4.

Stopped-flow UV/Vis measurements of (A) Mn^{II}-FeBMb(Fe^{II}) and (B) Co^{II}-FeBMb(Fe^{II}) upon reaction with O_2-saturated 100mM potassium phosphate pH 6 buffer between 1ms and 300s. The coloring order of each trace (from earliest to latest) is black (1ms) → green (for Mn^{II}-FeBMb(Fe^{II}), 20ms) → blue (600ms) → red (300s).

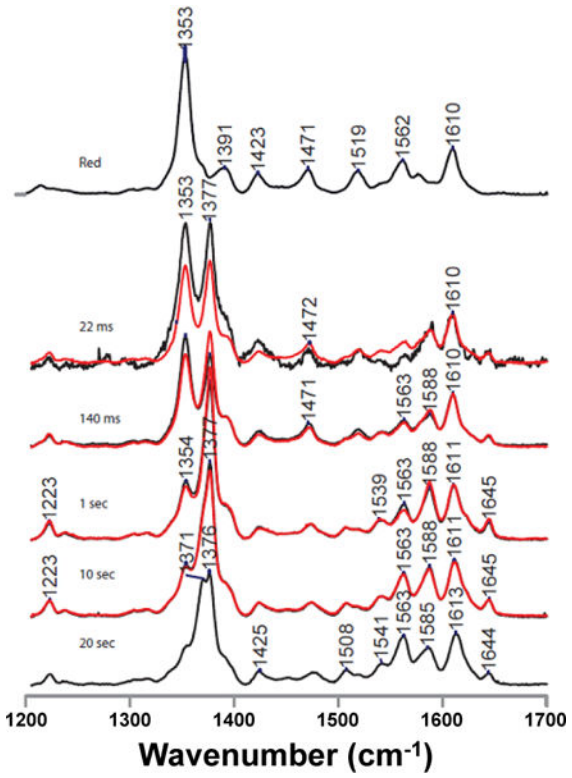

Figure 5.

Resonance Raman spectra of rapid freeze quench samples of Co^{II}–FeBMb(Fe^{II}) prepared upon reaction with $^{16}O_2$- (black) or $^{18}O_2$-saturated (red) buffer.

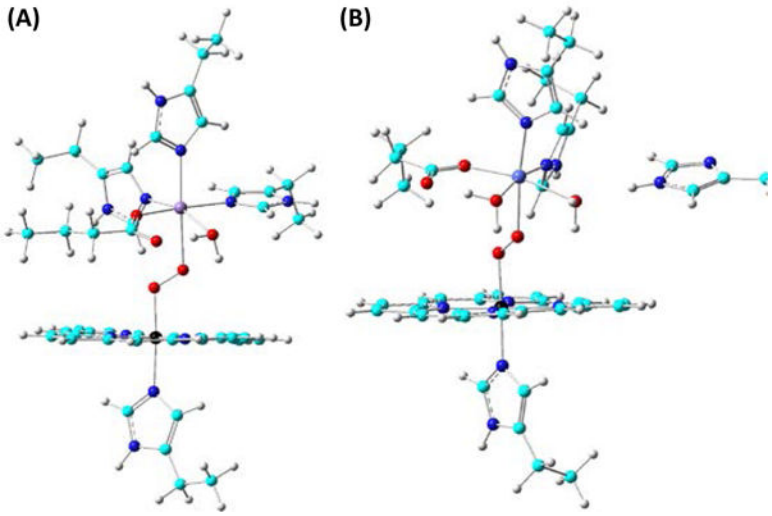

Figure 6.

Optimized oxy-bound structures for (A) Mn^{II}- and (B) Co^{II}-FeBMb(Fe^{II}) proteins. Color scheme: C – cyan, N – blue, O– red, H – grey, Fe – black, Mn – light purple, Co – navy blue.

Table 1

Bond lengths of nonheme metal ligands

Fe_BMb variants	M-N_{H29} (Å)	M-N_{H43} (Å)	M-N_{H64} (Å)	M-$O1_{E68}$ (Å)	M-$O2_{E68}$ (Å)	M-H_2O (Å)
Fe^{II}	2.18	2.12	2.2	2.19	3.28	2.11
Mn^{II}	2.24	2.37	2.28	2.13	3.17	2.33
Co^{II}	2.05	4.04	2.18	2.36	2.12	2.12 & 2.34

M-N_{H29}, -NH43, -NH_{64}, $O1_{E68}$, $O2_{E68}$, and M-H_2O are the bond lengths of nonheme metal and their respective coordinating amino acid residue atoms, as well as water molecules. The Co^{II} variant is coordinated by 2 waters, and as such both bond lengths are given. NH43 of the Co^{II} structure is coordinated to the second H_2O molecule with bond length 2.38 Å.

Table 2

Bond length of O_2-added variants

Fe_BMb variants	R_{Fe-O} (Å)	R_{M-O} (Å)	R_{O-O} (Å)
E	1.869	/	1.277
Mn^{II}	1.883	2.400	1.301
Co^{II}	1.894	2.126	1.303
Fe^{II}	1.843	1.997	1.334